RADIOWAVE PROPAGATION GROUND EFFECTS

Radiowave propagation plays an important role in modern communication, radar, and navigation systems. The mathematical theory of radiowave propagation is based on Maxwell's equations (1), which were formulated by James Clerk Maxwell in the 1860s (2). The first free-space radiowave transmission experiments between a pair of antennas were performed by Heinrich Hertz in the 1880s (3). In 1897 Marconi first patented a wireless telegraphy system based on long-distance, radiowave propagation.

RADIOFREQUENCY SPECTRUM

Table 1 summarizes the frequency range, propagation characteristics, and applications of the letter-designated bands of the radiofrequency spectrum. The lower and upper bounds of the radiofrequency spectrum in Table 1 are somewhat arbitrary, but the indicated frequency range, 3 Hz to 300 GHz, encompasses the portion of the electromagnetic spectrum for which conventional antennas are used to transmit and receive radio waves. Some of the characteristics of the individual bands are as follows.

Extremely Low Frequency

Because free-space, extremely low frequency (ELF) wavelengths are extremely long (greater than 100 km), antennas are very inefficient radiators because they are electrically small. The other major disadvantage of ELF is lack of bandwidth for information transmission. Despite these disadvantages, ELF is useful for worldwide communication with submarines because the long wavelengths have a useful penetration depth (also called skin depth) of several tens of meters in sea water. In addition, the earth and the ionosphere support a low-attenuation waveguide mode at ELF (4) so that a wave, once launched, will propagate around the world with little loss of intensity. The ionosphere is the part of the upper atmosphere where sufficient ionization exists to affect radiowave propagation, and these effects are covered thoroughly in Ref. 5. The earth-ionosphere waveguide can actually support cavity modes with resonances (6) in the ELF range, and these resonances (called Schumann resonances)

Table 1. The Radiofrequency Spectrum

Frequency Range	Band	Characteristics	Applications
3 Hz–3 kHz	ELF	Long wavelength; inefficient antennas; earth-ionosphere waveguide; penetration of ground and sea water	Submarine communications; underground mine communications; geophysics
3–30 kHz	VLF	Large transmitting antennas; earth-ionosphere waveguide	Long-range communication; navigation, and time-frequency dissemination; geophysics
30–300 kHz	LF	Earth-ionosphere waveguide; high atmospheric noise	Navigational beacons
300 kHz–3 MHz	MF	Ground wave; ionospheric reflections (at night)	AM broadcasting; maritime communications
3–30 MHz	HF	Long-distance ionospheric propagation; maximum usable frequency	Maritime and aeronautical communications; citizens band and amateur radio
30–300 MHz	VHF	Line-of-sight propagation; ionosphere scatter; meteor scatter	Television and FM broadcasting; air traffic control; navigation
300 MHz–3 GHz	UHF	Line-of-sight propagation	Television broadcast; radar; satellite communication; mobile communication; global positioning system
3–30 GHz	SHF	Line-of-sight propagation; atmospheric absorption	Radar; satellite communication; microwave links
30–300 GHz	EHF	Line-of-sight propagation; severe atmospheric absorption	Radar; secure communication; satellite links

further enhance the field strength worldwide. Unfortunately, these resonances also enhance the competing atmospheric noise caused by thunderstorms.

ELF waves have an even larger skin depth (typically greater than 100 m) in ground or rock (which have lower electrical conductivities than sea water) and have been found useful for communication to and within underground mines (7). Because of this ability to penetrate rock, ELF waves have also been used in direction-finding applications for location of miners trapped in underground mines (8).

Very Low Frequency

The free-space wavelengths at very low frequency (VLF) are still very long (10 to 100 km), and this generally dictates the use of large vertical transmitting antennas with large ground systems to reduce ground current losses. Smaller antennas, such as vertical whips, loops, and grounded horizontal wires, can be used for receiving. VLF antennas and propagation are thoroughly covered in Ref. 9.

Even though the bandwidth is limited, VLF systems are useful for long-range reliable communications, long-range dissemination of standards for frequency and time, long-range navigation (including the U.S. Navy Omega system), and geophysical probing of the ground and the ionosphere. For short ranges, VLF propagates predominantly by the ground wave. For long ranges, the reflections from the ionosphere become important, and multiple reflections between the earth and the ionosphere can be described by earth-ionosphere waveguide modes (9).

Low Frequency

The low frequency (LF) band is also characterized by low attenuation of ground wave propagation and earth-ionosphere waveguide propagation. Thus the LF band is useful for long-range communication and for marine and aeronautical radio navigation beacons. The LORAN-C navigation system is based on the arrival time of a ground-wave pulse with a carrier frequency of approximately 100 kHz so that later-arriving ionospheric reflections do not affect the system. The wavelengths are long enough (1–10 km) that large transmitting antennas are needed.

Medium Frequency

The most popular use of the medium frequency (MF) band is AM broadcasting, which uses the frequency range from 535 to 1705 kHz. The propagation mode is generally vertically polarized ground wave, although ionospheric reflections (sky wave) can extend the range at night. Maritime communications is another application.

High Frequency

In the high frequency (HF) band, ionospheric reflections provide the possibility of long-distance communications. The maximum usable frequency (MUF) for ionospheric reflection generally occurs in the upper part of the HF band, but the MUF is a complicated function of the incidence angle and the state of the ionosphere (5). HF applications include maritime, aeronautical, amateur, and citizens-band communications.

Very High Frequency

At frequencies above 30 MHz, propagation is predominantly by line of sight with some refraction (bending) caused by the atmosphere. However, in some cases ionospheric reflections can occur at frequencies up to 60 MHz. Scattering from ionized meteor trails (which can be up to 25 km in length) can be used for meteor burst communications (10). Very high frequency (VHF) applications include television and FM radio broadcasting and air traffic control and navigation.

Ultra High Frequency

Ultra high frequency (UHF) propagation is essentially by line of sight with some atmospheric refraction and some scattering by ionospheric irregularities. Applications include UHF television broadcasting, various radars, satellite communications, and personal communications (11). The global positioning system (GPS) uses transmitting satellites in the UHF band.

Super High Frequency

Super high frequency (SHF) propagation is primarily line of sight, and atmospheric absorption becomes significant, particularly above 10 GHz. A water vapor absorption line exists at approximately 21 GHz, and rain absorption and scattering increase with frequency throughout the band. SHF applications include radar, satellite communication, and microwave links.

Extremely High Frequency

The extremely high frequency (EHF) band is also called the millimeter-wave spectrum since the wavelength ranges from 1 to 10 mm. Atmospheric absorption becomes extreme in this band. An oxygen absorption band is centered at approximately 60 GHz, and numerous absorption peaks due to oxygen and water vapor occur above 100 GHz. Rain attenuation is significant throughout the entire EHF band. Satellite-to-satellite links are not affected by atmospheric absorption, and secure short-range communication systems take advantage of high attenuation to limit propagation range.

LINE-OF-SIGHT PROPAGATION

Line of sight is the dominant mode of propagation for elevated antennas and high frequencies, as indicated Table 1. The mathematical description of line-of-sight propagation is most easily obtained by considering simple antennas in a free-space environment. In this section two classical cases are discussed. First a Hertzian dipole source is considered to illustrate radiation of a spherical wave. Then transmission between a pair of antennas is analyzed to derive the classical expression for basic free-space transmission loss.

Radiation from a Hertzian Dipole

This article covers only steady-state, time-harmonic sources and fields (12) with time variation $\exp(j\omega t)$, where the angular frequency $\omega = 2\pi f$ and f is the radio frequency. The time dependence is suppressed in the equations. The basic source is a current I extending over an incremental length l. This elementary dipole source is called a Hertzian dipole and has a moment Il. If the dipole is directed along the z axis, as shown in Fig. 1, the radiated electric field has two components, E_θ and E_r, and the radiated magnetic field has only a single component H_ϕ. The expressions for these field components can be derived from scalar and vector potentials (12):

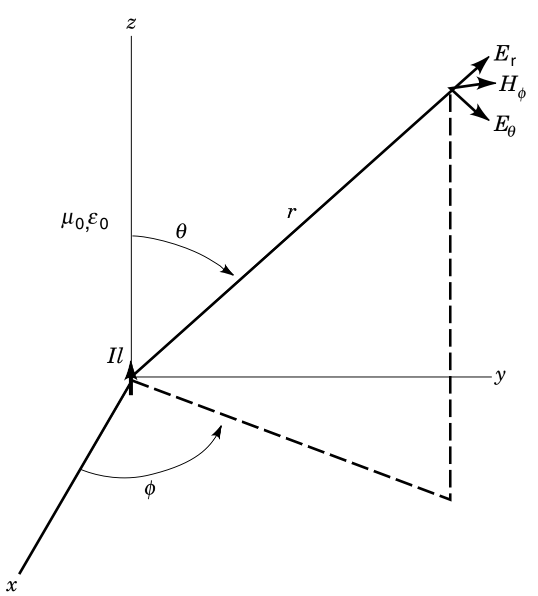

Figure 1. Geometry for radiation from a short electric dipole.

$$E_\theta = \frac{Il\eta_0}{4\pi} e^{-jk_0 r}\left(\frac{jk_0}{r} + \frac{1}{r^2} + \frac{1}{jk_0 r^3}\right)\sin\theta \tag{1}$$

$$E_r = \frac{Il\eta_0}{2\pi} e^{-jk_0 r}\left(\frac{1}{r^2} + \frac{1}{jk_0 r^3}\right)\cos\theta \tag{2}$$

$$\text{and } H_\phi = \frac{Il}{4\pi} e^{-jk_0 r}\left(\frac{jk_0}{r} + \frac{1}{r^2}\right)\sin\theta \tag{3}$$

where the free-space wave number $k_0 = \omega\sqrt{\mu_0\epsilon_0}$, the free-space impedance $\eta_0 = \sqrt{\mu_0/\epsilon_0}$, μ_0 is the magnetic permeability of free space, and ϵ_0 is the dielectric permittivity of free space. The equations for radiation by the dual source (a magnetic dipole or small loop) are given in Ref. 12.

Very close ($k_0 r \ll 1$) to the Hertzian dipole, the electric field is dominated by the r^{-3} inverse cube term, and Eqs. (1) and (2) can be approximated by

$$E_\theta \approx \frac{Il\sin\theta}{4\pi j\omega\epsilon_0 r^3} \text{ and } E_r \approx \frac{Il\cos\theta}{2\pi j\omega\epsilon_0 r^3} \tag{4}$$

Equation (4) gives the electric field components of charges $\pm I/j\omega$ separated by a distance l. The magnetic field of an electric dipole has no quasi-static term. At intermediate distances ($k_0 r \approx 1$), the inverse-square terms dominate Eqs. (1)–(3), and the field is called the induction field.

For most practical applications, such as communications or radar, the far fields are of interest. At large distances ($k_0 r \gg 1$), the inverse-distance terms dominate Eqs. (1) and Eq. (3), and the fields are approximated by

$$H_\phi \approx \frac{jk_0 Il}{4\pi r} e^{-jk_0 r}\sin\theta \text{ and } E_\theta \approx \eta_0 H_\phi \tag{5}$$

Even though Eq. (5) applies to a Hertzian dipole, it illustrates the more general far-field properties that the electric and magnetic fields are related by the free-space impedance and they are orthogonal to each other and to the radial direction of propagation. Hence the radial electric field E_r in Eq. (2) has no inverse-distance term.

The power density of the electromagnetic field is called the Poynting vector $\boldsymbol{S}$ and can be written

$$\boldsymbol{S} = \boldsymbol{E} \times \boldsymbol{H}^* \tag{6}$$

where boldface denotes vectors and * denotes complex conjugate. The far-field expression for $\boldsymbol{S}$ can be obtained by substituting Eq. (5) into Eq. (6):

$$\boldsymbol{S} \approx \hat{\boldsymbol{r}}\eta_0\left(\frac{k_0|I|l\sin\theta}{4\pi r}\right)^2 \tag{7}$$

where $\hat{\boldsymbol{r}}$ is the unit vector in the radial direction. The $\sin^2\theta$ factor in Eq. (7) is specific to the radiation pattern of a Hertzian dipole, but the inverse-square dependence applies to the far field of any radiator. The total radiated power P can be obtained by integrating Eq. (7) over a far-field sphere (12):

$$P = \int_0^{2\pi} d\phi \int_0^{\pi} d\theta\, r^2 \sin\theta \hat{\boldsymbol{r}} \cdot \boldsymbol{S} = \frac{\eta_0 (k_0 |I| l)^2}{6\pi} \tag{8}$$

The result for the total radiated power in Eq. (8) is independent of the radius r at which the integration is evaluated, but the evaluation is simplest in the far field, where $\boldsymbol{S}$ can be approximated by Eq. (7).

Free-Space Transmission Loss

Now consider free-space transmission between a pair of antennas in the far fields of each other. The received power P_r can be written (13)

$$P_r = \frac{P_t G_t G_r}{(2k_0 D)^2} = \frac{P_t G_t G_r \lambda_0^2}{(4\pi D)^2} \tag{9}$$

where P_t is the transmitted power, G_t is the gain of the transmitting antenna, G_r is the gain of the receiving antenna, D is the separation distance between the antennas, and the free-space wavelength $\lambda_0 = 2\pi/k_0$. The D^{-2} factor represents the inverse-square dependence of the radiated power density available at the receiving antenna.

The antenna and propagation effects can be separated by writing Eq. (9) in the following form:

$$\frac{P_r}{P_t} = G_t G_r \left(\frac{\lambda_0}{4\pi D}\right)^2 \tag{10}$$

The squared factor on the right side of Eq. (10) is dimensionless and does not involve the antenna gains. The reciprocal is called the free-space transmission loss L_0 and is usually expressed in decibels:

$$L_0 = 10\log_{10}\left(\frac{4\pi D}{\lambda_0}\right)^2 \text{ dB} = 20\log_{10}\left(\frac{4\pi D}{\lambda_0}\right) \text{ dB} \tag{11}$$

Normally the antenna gains and the power ratio in Eq. (10) are also expressed in decibels.

REFLECTION FROM A PLANAR INTERFACE

Plane-Wave Incidence

Radio waves are often reflected from smooth, flat surfaces, such as building walls or ground. When the reflecting surface is not a perfect conductor, part of the radio energy penetrates the surface, and part of the energy is reflected. Reflection of a plane wave from a uniform half space with a planar interface can be analyzed exactly by matching boundary conditions at the interface, and the derived reflection coefficients can then be used in other practical applications.

Consider the idealized geometry in Fig. 2. A free-space plane wave propagating at an angle θ_0 to the surface normal is incident on a half space with permittivity ϵ, electrical conductivity σ, and permeability μ. The angle of reflection θ_r equals the angle of incidence, $\theta_r = \theta_0$. The reflection coefficient depends on the polarization of the incident field.

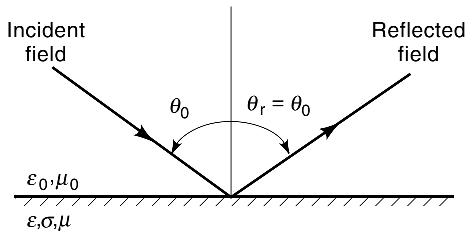

Figure 2. Geometry for plane-wave reflection from a homogeneous half space.

For horizontal polarization (electric field perpendicular to the plane of incidence), the reflection coefficient Γ_h is given by (1)

$$\Gamma_h = \frac{\mu k_0 \cos\theta_0 - \mu_0\sqrt{k^2 - k_0^2 \sin^2\theta_0}}{\mu k_0 \cos\theta_0 + \mu_0\sqrt{k^2 - k_0^2 \sin^2\theta_0}} \tag{12}$$

where $k = \omega\sqrt{\mu(\epsilon - j\sigma/\omega)}$. For vertical polarization (electric field parallel to the plane of incidence), the reflection coefficient Γ_v is

$$\Gamma_v = \frac{\mu_0 k^2 \cos\theta_0 - \mu k_0\sqrt{k^2 - k_0^2 \sin^2\theta_0}}{\mu_0 k^2 \cos\theta_0 + \mu k_0\sqrt{k^2 - k_0^2 \sin^2\theta_0}} \tag{13}$$

The reflection coefficients in Eq. (12) and (13) apply to both the reflected electric and magnetic fields. The power reflection coefficients are obtained by taking the squares of the magnitudes of the field reflection coefficients, $|\Gamma_v|^2$ and $|\Gamma_h|^2$. In general, the reflection coefficients in Eqs. (12) and (13) are complex because k is complex. Thus the reflected field undergoes phase shift as well as reduction in amplitude. In the limiting case of grazing incidence ($\theta_0 = \pi/2$), both Γ_h and Γ_v equal -1.

For the common case where the reflecting medium is nonmagnetic ($\mu = \mu_0$), the reflection coefficients in Eqs. (12) and (13) simplify to

$$\Gamma_h = \frac{\cos\theta_0 - \sqrt{(k/k_0)^2 - \sin^2\theta_0}}{\cos\theta_0 + \sqrt{(k/k_0)^2 - \sin^2\theta_0}} \tag{14}$$

and

$$\Gamma_v = \frac{(k/k_0)^2\cos\theta_0 - \sqrt{(k/k_0)^2 - \sin^2\theta_0}}{(k/k_0)^2\cos\theta_0 + \sqrt{(k/k_0)^2 - \sin^2\theta_0}} \tag{15}$$

For the further simplification to a dielectric ($\sigma = 0$) reflecting medium, Eqs. (14) and Eq. (15) reduce to

$$\Gamma_h = \frac{\cos\theta_0 - \sqrt{\epsilon_r - \sin^2\theta_0}}{\cos\theta_0 + \sqrt{\epsilon_r - \sin^2\theta_0}} \tag{16}$$

and

$$\Gamma_v = \frac{\epsilon_r\cos\theta_0 - \sqrt{\epsilon_r - \sin^2\theta_0}}{\epsilon_r\cos\theta_0 + \sqrt{\epsilon_r - \sin^2\theta_0}} \tag{17}$$

where $\epsilon_r = \epsilon/\epsilon_0$.

As incidence angle θ_0 varies from 0 (normal incidence) to $\pi/2$ (grazing incidence), Γ_h varies smoothly from $(1 - \sqrt{\epsilon_r})/(1 + \sqrt{\epsilon_r})$ to -1. However, for vertical polarization, the reflection coefficient Γ_v equals 0 at the Brewster angle, $\theta_B = \tan^{-1}(\sqrt{\epsilon_r})$. At this angle, all of the incident energy is refracted into the dielectric. An examination of Eq. (15) reveals that the presence of nonzero conductivity σ (which yields a complex k) prevents Γ_v from going to zero. However, if the imaginary

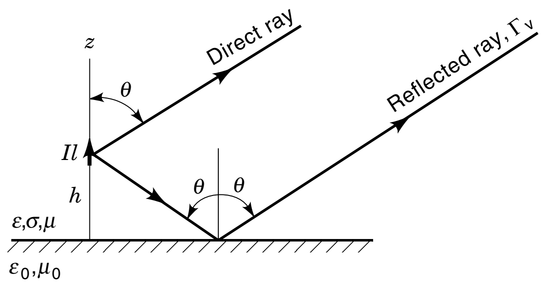

Figure 3. Far-field radiation from a vertical electric dipole over a homogeneous half space. The reflection coefficient Γ_v is a function of the incidence angle θ.

part of k is small, there is nevertheless a pseudo-Brewster angle (14) where $|\Gamma_v|$ goes through a minimum.

Dipole Sources

Consider now a vertical electric dipole source located at a height h over a reflecting half space, as in Fig. 3. In the far field the electric field has only a θ component E_θ, which can be written as the sum of a direct and a reflected ray:

$$E_\theta = \frac{j\omega\mu_0 Il \sin\theta}{4\pi r} e^{-jk_0 r}(e^{jk_0 h\cos\theta} + \Gamma_v e^{-jk_0 h\cos\theta}) \tag{18}$$

where Γ_v is given by Eq. (13). For the special case of a perfectly conducting ground plane ($\sigma = \infty$), the reflection coefficient equals 1, and Eq. (18) reduces to

$$E_\theta|_{\sigma=0} = \frac{j\omega\mu_0 Il \sin\theta}{2\pi r} e^{-jk_0 r}\cos(k_0 h\cos\theta) \tag{19}$$

Equation (19) has a maximum at the interface, $\theta = \pi/2$.

The dual case of a vertical magnetic dipole source is shown in Fig. 4. The source is a small loop of area A and current I, and the loop axis is in the vertical direction. The electric field is horizontally polarized, and in the far field the ϕ component E_ϕ is

$$E_\phi = \frac{\eta_0 k_0^2 IA \sin\theta}{4\pi r} e^{-jk_0 r}(e^{jk_0 h\cos\theta} + \Gamma_h e^{-jk_0 h\cos\theta}) \tag{20}$$

where Γ_h is given by Eq. (12). For the special case of a perfectly conducting ground plane ($\sigma = \infty$), the reflection coefficient equals -1, and Eq. (20) reduces to

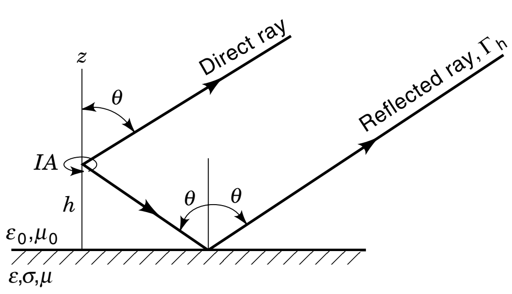

Figure 4. Far-field radiation from a vertical magnetic dipole over a homogeneous half space. The reflection coefficient Γ_h applies to horizontal polarization.

$$E_\phi|_{\sigma=\infty} = \frac{j\eta_0 k_0^2 IA \sin\theta}{2\pi r} e^{-jk_0 r}\sin(k_0 h\cos\theta) \tag{21}$$

Equation (21) has a null at the interface, $\theta = \pi/2$.

For realistic (finite) ground parameters, the reflection coefficients for both vertical polarization Γ_v and horizontal polarization Γ_h equal -1 at grazing incidence ($\theta = \pi/2$). Hence the direct and reflected rays cancel in Eqs. (18) and (20), and the electric field is 0:

$$E_\theta|_{\theta=\pi/2} = 0 \text{ and } E_\phi|_{\theta=\pi/2} = 0 \tag{22}$$

In reality, only the space wave (the inverse-distance field that occurs for $\theta > 0$) is 0 at the interface. The ground wave is the dominant field component near the interface, and it will be discussed in detail later. It has a more rapid decay with distance, but it does not equal 0 at the interface.

PLANE-WAVE REFRACTION

Dielectric Medium

Consider a plane wave incident on a dielectric half space, as in Fig. 5. For simplicity, the dielectric is taken to be lossless ($\sigma = 0$) and nonmagnetic ($\mu = \mu_0$). The incident field propagates at an angle θ_0 to the normal, and the transmitted field is refracted at an angle θ_t to the normal. The angle of refraction is determined by requiring that the phases of the refracted field and the incident field maintain the same relationship at all points along the interface. This requirement is met if the tangential wave numbers in the two media are equal: $k_0 \sin\theta_0 = k \sin\theta_t$. For the case of a dielectric medium, this reduces to

$$\frac{\sin\theta_t}{\sin\theta_0} = \sqrt{\frac{\epsilon_0}{\epsilon}} \text{ or } \theta_t = \sin^{-1}\left(\frac{\sin\theta_0}{n}\right) \tag{23}$$

where $n = \sqrt{\epsilon/\epsilon_0} = \sqrt{\epsilon_r}$ is the refractive index. Equation (23) is called Snell's law (14). As with the reflection coefficient,

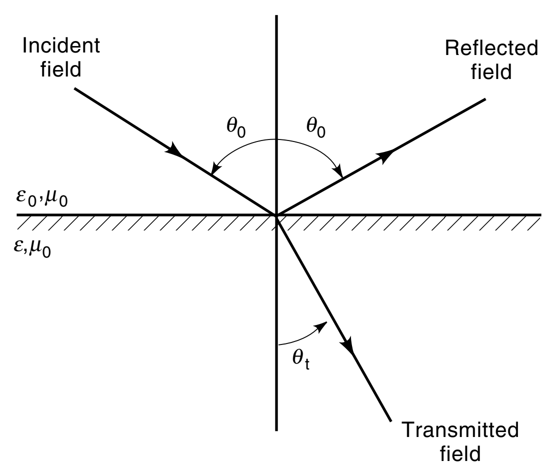

Figure 5. Reflection from and refraction into a dielectric half space. The diffraction angle θ_t is determined from Snell's law.

the transmission coefficient depends on the polarization of the incident field.

For horizontal polarization (electric field perpendicular to the plane of incidence), the electric-field transmission coefficient T_h is given by (1)

$$T_{\mathrm{h}} = \frac{2\cos\theta_0}{\cos\theta_0 + \sqrt{\epsilon_{\mathrm{r}} - \sin^2\theta_0}} \tag{24}$$

For vertical polarization (electric field parallel to the plane of incidence), the electric field transmission coefficient T_v is given by (1)

$$T_{\mathrm{v}} = \frac{2\sqrt{\epsilon_{\mathrm{r}}}\cos\theta_0}{\epsilon_{\mathrm{r}}\cos\theta_0 + \sqrt{\epsilon_{\mathrm{r}} - \sin^2\theta_0}} \tag{25}$$

The magnetic field transmission coefficients are obtained by multiplying the electric field transmission coefficients in Eqs. (24) and (25) by $\sqrt{\epsilon_r}$.

Lossy Medium

Transmission into a lossy medium at oblique incidence is complicated by the fact that the planes of constant phase do not coincide with the planes of constant amplitude. Such a transmitted field is called an inhomogeneous plane wave (1). To simplify the mathematics, the case of normal incidence, as shown in Fig. 6, will be considered.

For normal incidence the electric field is transverse to the z direction. The incident electric field E^i in the free-space region ($z > 0$) has unit amplitude:

$$E^{\mathrm{i}} = \exp(jk_0 z) \tag{26}$$

The reflected electric field E^r in the free-space region is

$$E^{\mathrm{r}} = \Gamma_{\mathrm{h}}|_{\theta_0=0}\exp(-jk_0 z) \tag{27}$$

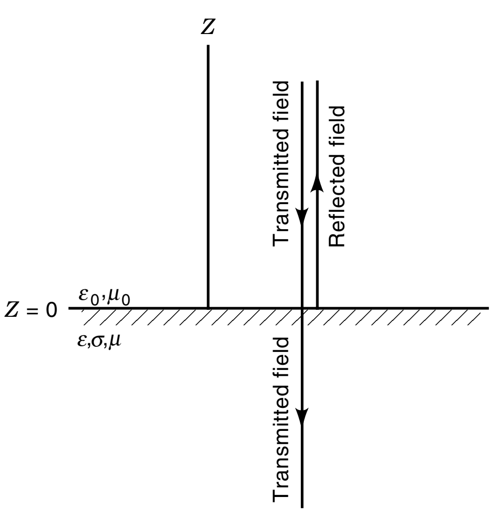

Figure 6. Reflection from and transmission into a lossy half space for normal incidence.

where Γ_h is given by Eq. (12). The transmitted electric field E^t in the lossy medium ($z < 0$) is

$$E^{\mathrm{t}} = T\exp(jkz), \text{ where } k = \omega\sqrt{\mu(\epsilon - j\sigma/\omega)} \tag{28}$$

The transmission coefficient T is given by

$$T = \frac{2\mu k_0}{\mu k_0 + \mu_0 k} \tag{29}$$

Equation (29) can be written compactly in terms of impedances:

$$T = \frac{2\eta}{\eta + \eta_0} \tag{30}$$

where η_0 is the free-space impedance and $\eta = \sqrt{\mu/(\epsilon - j\sigma/\omega)}$ is the impedance of the lossy medium. In general, T is complex, and the transmitted field undergoes both phase shift and reduction in amplitude.

As the transmitted field propagates into the lossy medium, it undergoes further attenuation and phase delay, as indicated by Eq. (28). The attenuation and phase shift can be isolated by normalizing the field to the value at the interface:

$$\frac{E^{\mathrm{t}}}{T} = \exp[\mathrm{Im}\,(k)d]\exp[-j\mathrm{Re}(k)d] \tag{31}$$

where Re indicates real part, Im indicates imaginary part, and $d = -z$ is the depth in the medium. The first exponential factor on the right side of Eq. (31) represents attenuation, and the second factor represents phase shift.

The skin depth δ is defined as the distance over which the amplitude of the field decreases to $1/e$ times its initial value. The expression for δ is

$$\delta = \frac{-1}{\mathrm{Im}(k)} = \sqrt{\frac{2}{\sqrt{a^2 + b^2} - a}}, \text{ where } a = \omega^2\mu\epsilon \text{ and } b = \omega\mu\sigma \tag{32}$$

For a lossless medium ($\sigma = b = 0$), the skin depth δ is ∞ (no attenuation).

For the case where conduction currents dominate displacement currents ($\sigma \gg \omega\epsilon$), Eq. (32) simplifies to

$$\delta \approx \sqrt{\frac{2}{\omega\mu\sigma}} = \sqrt{\frac{1}{\pi f\mu\sigma}} \tag{33}$$

Equation (33) applies to high-conductivity metals, such as copper, and to soil and rock at low frequencies.

THROUGH-THE-EARTH PROPAGATION

The antenna and propagation issues are similar for subsurface communications (7) and geophysical probing of the earth (15). Both applications require transmission of electromagnetic waves through the earth, and both face the problem of high attenuation. To penetrate the earth to depths of 100 m or more, it is necessary to employ frequencies below about 3 kHz (ELF). The reason for this is that the skin depth is proportional to $1/\sqrt{f}$, as indicated in Eq. (33). Although plane-

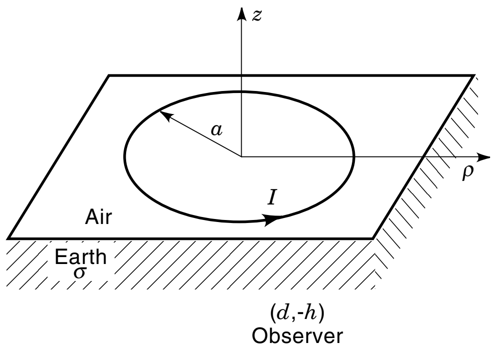

Figure 7. Circular loop on a conducting half space with a subsurface observer.

wave propagation as discussed in the previous section gives valid results for distant sources, it does not give valid quantitative results for the typical case where the transmitting antenna is located at or below the air-earth interface. So this section will deal with the fields of surface or buried antennas.

At frequencies below 3 kHz, the free-space wavelength is greater than 100 km. Consequently, ELF antennas are electrically small even though they could be physically large. The methods and antennas used in geophysical probing are too varied to give a complete description. However, if we limit the applications to deep, subsurface probing and to through-the-earth communication, then the most useful antennas are of two types: wire loop antennas and straight wire antennas grounded at the ends.

Fields of Loop Antennas

Loop antennas are commonly used in geophysical sounding and subsurface communications, and they have the advantage that no grounding is required. In geophysical sounding, loop antennas transmit a time-varying magnetic field into the earth, and eddy currents are excited in conducting bodies. These eddy currents generate a secondary magnetic field that can be received by a second loop antenna. In mine communications, transmitting loops can be used either at or below the earth surface. Horizontal transmitting loops are typically a large, single turn of wire laid out on the earth. Various shapes, such as circular or rectangular, are used depending on the application. When the loop dimensions are small compared with the skin depth in the earth and the observer distance, the horizontal loop radiates as a vertical magnetic dipole.

A circular loop of radius a located at the earth surface ($z = 0$) is shown in Fig. 7. The earth conductivity is σ, and the magnetic permeability of both the air and the earth is μ_0. For the low frequencies considered here, displacement currents are negligible, and the fields are independent of permittivity. This is called the quasi-static approximation and is obtained by setting the free-space wave number k_0 equal to 0. The wave number in the earth is approximated by $k \approx \sqrt{\omega\mu_0\sigma/j}$, where the square root is taken so that the imaginary part is negative.

When the circular loop carries a uniform current I, the nonzero field components are H_z, H_ρ, and E_ϕ. The vertical magnetic field H_z in the earth ($z < 0$) is of primary interest for downlink communication between horizontal loops. At a depth h and a horizontal distance d, H_z is given by (16)

$$H_z = \frac{IA}{2\pi h^3}Q \tag{34}$$

where

$$Q = \int_0^\infty \frac{g^3 e^{-\sqrt{g^2+jH^2}}}{g+\sqrt{g^2+jH^2}} J_0(gD)\frac{2J_1(ga/h)}{ga/h}dg \tag{35}$$

$H = \sqrt{\omega\mu_0\sigma}h$, $D = d/h$, and J_0 and J_1 are the zero- and first-order Bessel functions (17). The integration variable g is a normalized wave number; so the integration in Eq. (35) can be interpreted as the result of a superposition of all the waves that the loop antenna transmits into the earth. The exponential factor is consistent with skin depth attenuation because for small g it is given by $|\exp(-\sqrt{jH^2})| = \exp(-h/\delta)$, where δ is given by Eq. (33).

When $a/h \ll 1$, the factor $2J_1(ga/h)/(ga/h)$ approaches 1 over the significant range of g. In that case the dependence on a enters only on through the loop area $A(=\pi a^2)$, and the loop radiates like a magnetic dipole of moment IA. If the loop is buried at a depth h and the observer is located at the surface (as in uplink communications), the result for H_z is identical.

For the special case of $H = a/h = 0$, the quantity Q reduces to the following result for a static magnetic dipole:

$$Q|_{H=a/h=0} = \frac{2-D^2}{2(1+D^2)^{5/2}} \tag{36}$$

If, in addition, $D = 0$, then $Q = 1$. Thus Q is the vertical magnetic field normalized to the on-axis magnetic field of a static magnetic dipole. For $D = 0$, both H_ρ and E_ϕ are 0.

In general, the integration in Eq. (35) must be performed numerically. The infinite upper limit presents no practical difficulty because of the exponential decay for large g. Figure 8 shows the normalized vertical magnetic field magnitude $|Q|$ on the loop axis ($D = 0$) as a function of normalized depth H for a magnetic dipole source ($a/h = 0$). For large values of H, the field strength decays exponentially just as a plane wave does. For geophysical probing, vertical sounding (18) is accomplished by varying the frequency, and low frequencies are required to obtain information on earth conductivity at great depth.

In mine communication (7) and source location (8), the off-axis ($D > 0$) field is of interest. Figure 9 shows the dependence of the vertical magnetic field strength on normalized horizontal distance D. For the static case ($H = 0$), there is a null at $D = \sqrt{2}$, as shown in Eq. (36), and that null can be useful in source location (8). For nonzero values of H, Q is complex, and the null is filled in.

The magnetic field results in Figs. 8 and 9 are actually valid for small loops of any shape that can be represented by a magnetic dipole. When the loop dimensions are large, the field depends strongly on shape. The theory has been developed for loops of arbitrary shape in a conducting medium that is homogeneous or layered (19). Results for a loop of nonzero radius are shown in Fig. 10 for the static case ($H = 0$). As the loop radius is increased, the vertical magnetic field is reduced on the axis ($D = 0$), but is increased at the larger horizontal distances. A similar behavior occurs for nonzero values of H.

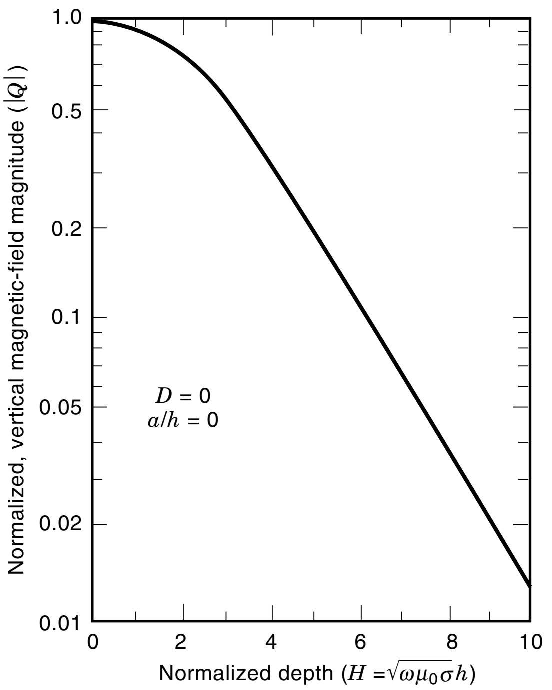

Figure 8. Magnitude of the normalized vertical magnetic field of a small circular loop ($a = 0$) as a function of the normalized depth H on the axis ($D = 0$). From Ref. 16.

Also, similar results have been calculated for rectangular loops (19).

Fields of Grounded Wire Antennas

Grounded wire antennas are the other antenna type commonly used to transmit fields through the earth. In addition

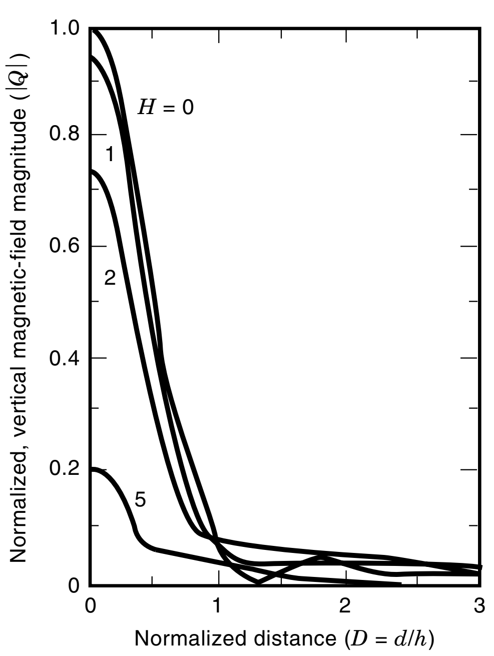

Figure 9. Magnitude of the normalized vertical magnetic field of a small circular loop ($a = 0$) as a function of the normalized horizontal distance D. From Ref. 16.

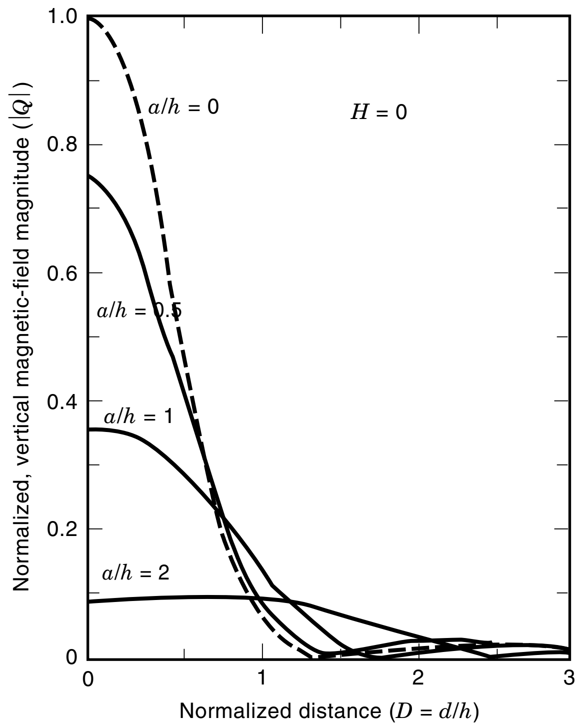

Figure 10. Magnitude of the normalized vertical magnetic field of a circular loop of radius a as a function of normalized distance D. From Ref. 16.

to geophysical sounding, these antennas are used for uplink and downlink communications in mines and for ELF communications with submarines (4). A typical configuration is shown in Fig. 11. The antenna is of length $2l$, and the current I is assumed to be constant over the length of the antenna. This assumption is valid for insulated antennas grounded at the ends when the length of the antenna is much less than a free-space wavelength (20). Because of the use of low frequencies, displacement currents are neglected in air and in the earth. The earth has conductivity σ and permeability μ_0.

The subsurface electric and magnetic fields are both of interest in mine communication and in probing of geophysical features. In mine communication, the subsurface magnetic

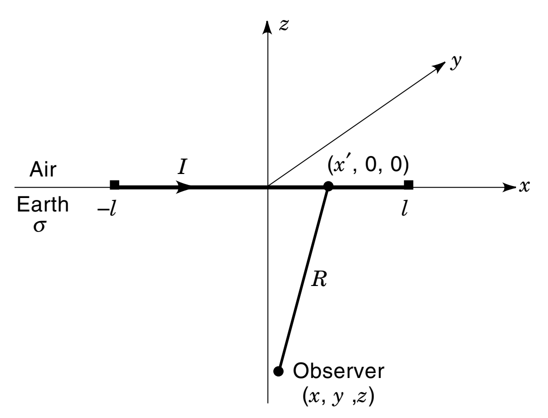

Figure 11. Electric line source on a conducting half space with a subsurface observer.

field is received with a loop antenna, or the subsurface electric field is received with a grounded wire antenna.

First consider the fields produced by an incremental current source of length dx' located at x', as shown in Fig. 11. Because of the quasi-static approximation, the Sommerfeld integral forms for an incremental source of current moment $I\,dx'$ can be greatly simplified (21). As a result, the magnetic field components are

$$dH_x = \frac{I\,dx'}{2\pi\gamma^2}\left(\frac{\partial^4 N}{\partial x\,\partial y\,\partial z^2} - \frac{\partial^3 P}{\partial x\,\partial y\,\partial z}\right) \tag{37}$$

$$dH_y = \frac{I\,dx'}{2\pi\gamma^2}\left(\frac{\partial^3 P}{\partial z^3} + \frac{\partial^3 P}{\partial x^2\,\partial z} + \frac{\partial^4 N}{\partial z^2\,\partial y^2}\right) \tag{38}$$

and

$$dH_z = \frac{I dx'}{2\pi\gamma^2}\left(\frac{\partial^4 N}{\partial y\,\partial z^3} - \gamma^2\frac{\partial^2 N}{\partial y\,\partial z} - \frac{\partial^3 P}{\partial y\,\partial z^2}\right) \tag{39}$$

where $N = I_0[(\gamma/2)(R + z)]K_0](\gamma/2)(R - z)]$, $P = R^{-1}\exp(-\gamma R)$, $R = \sqrt{(x-x')^2 + y^2 + z^2}, \gamma = \sqrt{j\omega\mu_0\sigma}$, and I_0 and K_0 are modified Bessel functions (17). Similarly, the electric field components are

$$dE_x = \frac{-I\,dx'}{2\pi\sigma}\left(\frac{\partial^2 P}{\partial z^2} + \frac{\partial^3 N}{\partial y^2\,\partial z}\right) \tag{40}$$

$$dE_y = \frac{I\,dx'}{2\pi\sigma}\frac{\partial^3 N}{\partial y\,\partial x\,\partial z} \tag{41}$$

and

$$dE_z = \frac{I\,dx'}{2\pi\sigma}\frac{\partial^2 P}{\partial x\,\partial z} \tag{42}$$

Although all six field components are, in general, nonzero, the dominant field components of interest are H_y, H_z, and E_x. These are the only nonzero components for a line source of infinite length, and all other field components vanish in the plane $x = 0$, even for a line source of finite length. To obtain the fields of the entire line source, Eqs. (38)–(40) must be integrated over the range of x' from $-l$ to l. For normalization purposes, it is convenient to write the fields in the following forms:

$$H_y = \frac{I}{2\pi h}A(H, Y, X, L) \tag{43}$$

$$H_z = \frac{I}{2\pi h}B(H, Y, X, L) \tag{44}$$

and

$$E_x = \frac{-j\omega\mu_0 I}{2\pi}F(H, Y, X, L) \tag{45}$$

where $H = \sqrt{\omega\mu_0\sigma}h$, $Y = y/h$, $X = x/h$, $L = l/h$, and $h = -z$. The normalized quantities A, B, F, H, Y, X, and L are dimensionless. The specific forms for the normalized fields are

$$A(H, Y, X, L) = \frac{h}{\gamma^2}\int_{-l}^{l}\left(\frac{\partial^3 P}{\partial z^3} + \frac{\partial^3 P}{\partial x^2\,\partial z} + \frac{\partial^4 N}{\partial z^2\,\partial y^2}\right)dx' \tag{46}$$

$$B(H, Y, X, L) = \frac{h}{\gamma^2}\int_{-l}^{l}\left(\frac{\partial^4 N}{\partial y\,\partial z^3} - \gamma^2\frac{\partial^2 N}{\partial y\,\partial z} - \frac{\partial^3 P}{\partial y\,\partial z^2}\right)dx' \tag{47}$$

and

$$F(H, Y, X, L) = \frac{1}{\gamma^2}\int_{-l}^{l}\left(\frac{\partial^2 P}{\partial z^2} + \frac{\partial^3 N}{\partial y^2\,\partial z}\right)dx' \tag{48}$$

The integral forms in Eqs. (46)–(48) simplify for both the low-frequency (small H) and high-frequency (large H) cases (21), but numerical integration is required in general. Typical numerical results for $H = 2$ are shown in Figs. 12–14. Although A, B, and F are complex for $H > 0$, only the magnitudes are plotted. The phases are relatively constant as a function of L. For very small values of L, the fields are essentially those of a short dipole and are proportional to L, as indicated by Eqs. (38)–(40). For large L, the field components eventually reach those of an infinite line source (22). The limits for large L are shown for the horizontal magnetic field as dashed lines in Fig. 12. In some geophysical applications, it is desirable to make the grounded wire long enough to simulate an infinitely long line source. An examination of Figs.

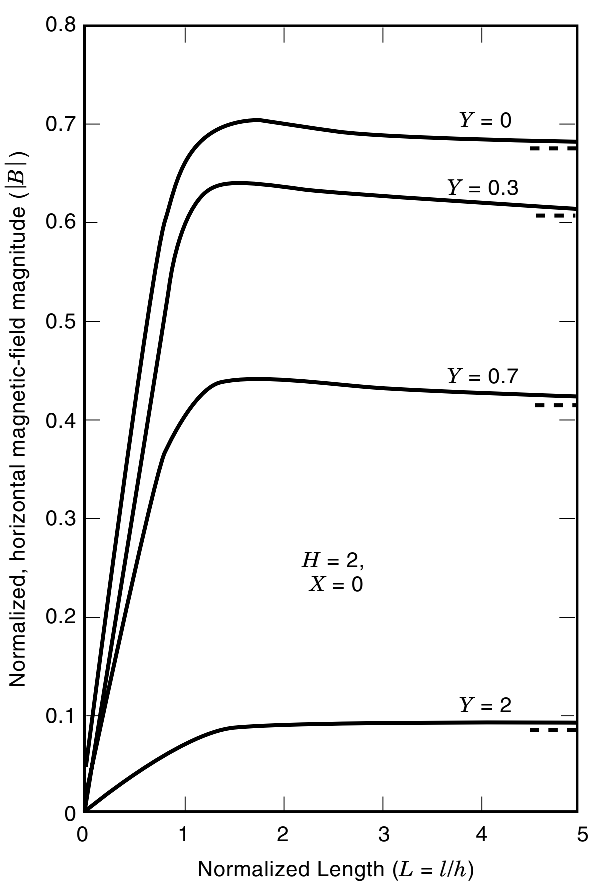

Figure 12. Magnitude of the normalized horizontal magnetic field as a function of the normalized line length L. The dashed lines indicate the limit, $L = \infty$. From Ref. 16.

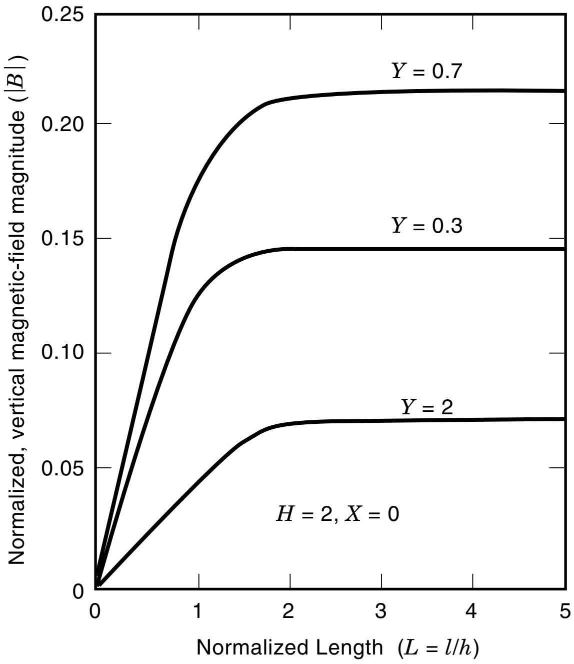

Figure 13. Magnitude of the normalized vertical magnetic field as a function of the normalized line length L From Ref. 16.

(11)–(14) and other calculations (21) shows that this is approximately achieved for L greater than about 2. This means that the antenna length $2l$ should be at least four times the depth h of interest in a particular geophysical application.

Straight, grounded wires are also used to excite broadband, transient fields in the earth. To illustrate the dispersive nature of the earth, it is useful to examine the frequency dependence of the subsurface electric fields. The frequency dependence of all three components of the electric field has been analyzed (23), but only the dominant component E_x, will be considered here. Equations (45) and (48) can be recast in the following equivalent form:

$$E_x = \frac{-I}{2\pi\sigma h^2} E_{xn}(W, L, X, Y) \tag{49}$$

where

$$E_{xn} = h^2 \int_{-l}^{l} \left(\frac{\partial^2 P}{\partial z^2} + \frac{\partial^3 N}{\partial y^2 \, \partial x} \right) dx' \tag{50}$$

and $W = \omega\mu_0\sigma h^2$. Equations (49) and (50) are consistent with Eqs. (45) and (48), but here the frequency dependence is explicitly displayed through the dimensionless frequency parameter W.

Some numerical results for $|E_{xn}|$ as a function of W are shown in Fig. 15. As W approaches 0, E_{xn} approaches the dc result E_{xn}^{dc}, which is obtained from the gradient of a scalar potential (23):

$$E_{xn}^{\mathrm{dc}} = (L - X)R_1^{-3} + (L + X)R_2^{-3} \tag{51}$$

where

$$R_1 = \sqrt{(X - L)^2 + Y^2 + 1} \text{ and } R_2 = \sqrt{(X + L)^2 + Y^2 + 1} \tag{52}$$

When W becomes large, $|E_{xn}|$ decreases exponentially because the skin depth becomes small.

Straight, grounded wire antennas are also used underground. For example, long wire antennas have been laid out in mine tunnels for uplink transmission. The surface fields of such antennas have been computed for the general case where the antenna is not parallel to the air-earth interface (24) to model cases where either the tunnel or the earth surface is not level.

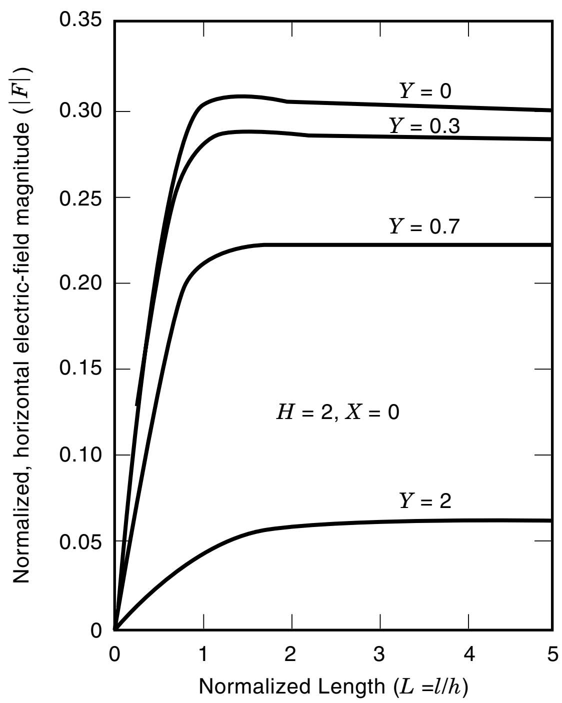

Figure 14. Magnitude of the normalized horizontal electric field as a function of the normalized line length L. From Ref. 16.

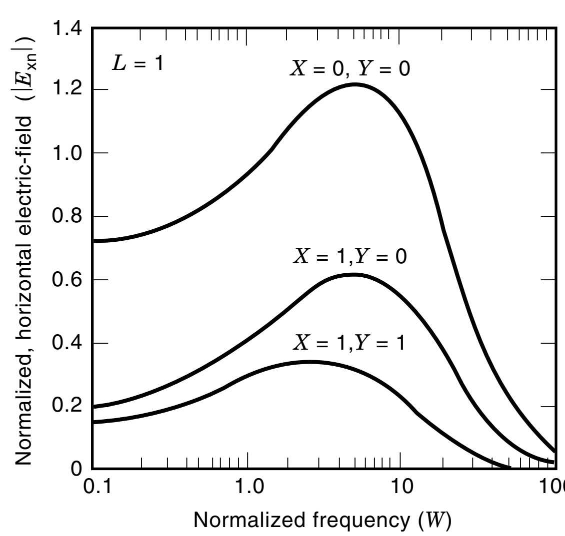

Figure 15. Magnitude of the normalized horizontal electric field of a horizontal line source as a function of the normalized frequency W.

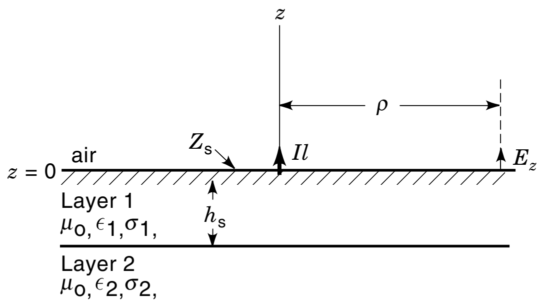

Figure 16. Vertical electric dipole source at the surface of a two-layer half space. The surface impedance Z_s depends on the properties of both layers.

GROUND-WAVE PROPAGATION

When both the transmitting and receiving antennas are located on the ground, the direct and reflected waves cancel. Consequently, the inverse-distance space wave is 0 as indicated in Eq. (22). In this case the ground wave is the dominant field component, and it can be calculated for either a flat-earth model or a curved-earth model.

Flat Earth

The flat-earth model is useful for analyzing propagation along flat surfaces (25) or curved surfaces with very large radii of curvature (such as the earth). Consider a vertical electric dipole (VED) source located at an impedance surface, as shown in Fig. 16. The air region has free-space permittivity ϵ_0, and free-space permeability μ_0 is assumed everywhere. The nonzero field components are E_z, E_ρ and H_ϕ.

For propagation analysis, the earth can be characterized by a surface impedance Z_s under fairly general conditions. The surface impedance is the ratio of the horizontal electric and magnetic fields at the earth surface: $Z_s = -(E_\rho/H_\phi)|_{z=0}$. For the two-layer model shown in Fig. 16, the surface impedance for grazing incidence (as in ground-wave propagation) is given by (26)

$$Z_s = Z_1 Q \tag{53}$$

where

$$Z_1 = \eta_1 \sqrt{1 - \frac{\eta_1^2}{\eta_0^2}} \tag{54}$$

$$Q = \frac{(u_2/u_1) + (\gamma_2^2/\gamma_1^2)\tanh u_1 h_1}{(\gamma_2^2/\gamma_1^2) + (u_2/u_1)\tanh u_1 h_1} \tag{55}$$

$$\eta_1 = \sqrt{\frac{\mu_0}{\epsilon_1 - j\sigma_1/\omega}},\ u_1 = \sqrt{\gamma_1^2 + k_0^2},\ u_2 = \sqrt{\gamma_2^2 + k_0^2},\ \gamma_1^2 = j\omega\mu_0(\sigma_1 + j\omega\epsilon_1)$$

and $\gamma_2^2 = j\omega\mu_0(\sigma_2 + j\omega\epsilon_2)$. The layer thickness h_1 and the layer constitutive parameters are defined in Fig. 16. Q is a correction factor to account for the layering, and $Q = 1$ for a homogeneous earth. For any passive earth model, the real part of the surface impedance must be nonnegative: $Re(Z_s) \geq 0$. For a homogeneous earth, the phase of Z_s ranges from 0 to $\pi/4$. For a layered earth, the phase of Z_s can range from $-\pi/2$ to $\pi/2$.

At large distances from the source ($k_0\rho \gg 1$), the dominant vertical electric field component E_z can be written (26)

$$E_z = \frac{-j\omega\mu_0 Il}{2\pi\rho} e^{-jk_0\rho} F(p) \tag{56}$$

where

$$F(p) = 1 - j\sqrt{\pi p}\, e^{-p}\ \mathrm{erfc}\ (j\sqrt{p}) \tag{57}$$

$p = (-jk_0\rho/2)\ \Delta^2$, $\Delta = Z_s/\eta_0$, and erfc is the complementary error function (17). The function $F(p)$ is called the Sommerfeld attenuation function and is actually a correction to the field of a vertical electric dipole located at the surface of a perfectly conducting plane. The quantity p is dimensionless and called the numerical distance. For $|p| \ll 1$, $F(p) \approx 1$.

For large numerical distance ($|p| \gg 1$), the asymptotic form of F depends on the phase of p (26):

$$F(p) \approx -\frac{1}{2p},\ -3\pi/2 \leq \text{ phase } (p) \leq 0 \tag{58}$$

or

$$F(p) \approx -2j\sqrt{\pi p}\, e^{-p} - \frac{1}{2p},\ 0 < \text{ phase } (p) \leq \pi/2 \tag{59}$$

The first term on the right side of Eq. (59) corresponds to a trapped surface wave (26) that can occur when the surface impedance is highly inductive (phase of $\Delta > \pi/4$). It does not occur for a homogeneous earth, as indicated in Eq. (58). If Eq. (58) is substituted into Eq. (56), the following result is obtained for the electric field:

$$E_z \approx \frac{\eta_0 Il}{2\pi\rho^2\Delta^2} e^{-jk_0\rho} \tag{60}$$

The ρ^{-2} dependence of the field in Eq. (60) is characteristic of a lateral wave that requires an interface to support it. A similar analysis is possible for horizontal polarization as produced by a horizontal electric dipole or vertical magnetic dipole source (26), but it is of less interest for ground-wave propagation because it decays more rapidly with distance than vertical polarization.

If the height of either the transmitting dipole or the observer is raised above the interface, the field is increased by a factor called the height-gain function G (26). Consider the case shown in Fig. 17, where both the source and observer are

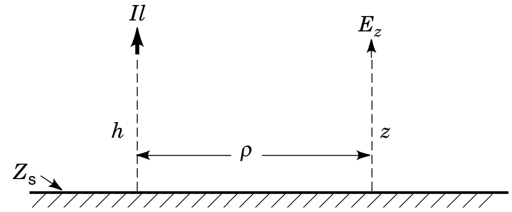

Figure 17. Elevated source and observer for propagation over a flat surface with surface impedance Z_s.

elevated. Then the electric field can be approximately written

$$E_z = \frac{-j\omega\mu_0 Il}{2\pi\rho} e^{-jk\rho} F(p)G(h)G(z) \tag{61}$$

where

$$G(h) = 1 + jk_0\Delta h \text{ and } G(z) = 1 + jk_0\Delta z \tag{62}$$

By reciprocity, the height-gain function G is the same for the source and observer. Equation (62) is valid only for small heights ($k_0|\Delta|h \ll 1$).

Spherical Earth

The spherical-earth model is used to account for diffraction loss that occurs for ground-wave propagation into the shadow region. The mathematical theory is complicated, but it has been well developed (26) and has been used to generate extensive numerical results for field strength as a function of distance, frequency, and earth surface properties (27–29). For short paths, the flat-earth and spherical-earth models give similar results, but for long paths the spherical-earth model must be used for accurate predictions.

The geometry for a radial electric dipole source located at the surface of a sphere of radius a is shown in Fig. 18. The surface is characterized by a surface impedance Z_s, which can be determined by Eqs. (53)–(55) for a layered earth. The nonzero field components are E_r, E_θ, and H_ϕ. The radial electric field E_r is the component of most interest, and its value at the surface ($r = a$) is

$$E_r = \frac{-j\omega\mu_0 Il}{2\pi d} e^{-jk_0 d} W \tag{63}$$

where d is the arc distance along the surface and W is the spherical-earth attenuation function. It is a correction to the field of a vertical electric dipole on a perfectly conducting plane in the same manner as F for the flat earth in Eq. (56). For large $k_0 a$ and $k_0 d$, W can be written as the classical residue series (25):

$$W = \sqrt{\frac{\pi x}{j}} \sum_{s=1}^{\infty} \frac{\exp(-jxt_s)}{t_s - q^2} \tag{64}$$

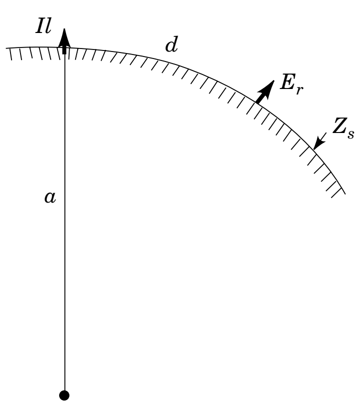

Figure 18. Vertical electric dipole source at the surface of a spherical earth with a surface impedance Z_s.

where $x = (k_0a/2)^{1/3}(d/a)$, $q = -j(k_0a/2)^{1/3}\ \Delta$, and $\Delta = Z_s/\eta_0$. The roots t_s satisfy the equation

$$w_1'(t_s) - qw_1(t_s) = 0 \tag{65}$$

where w_1 is an Airy function and w_1' is the derivative with respect to the argument. The Airy function w_1 is defined by

$$w_1(t) = \sqrt{\pi}[Bi(t) - jAi(t)] \tag{66}$$

where Ai and Bi are the Airy functions defined by Miller (30). A systematic method for determining the roots of Eq. (65) has been presented for arbitrary values of the magnitude and phase of q (27).

The residue series in Eq. (64) is valid for any value of x, but converges slowly for small values of x. Two alternative methods are available for the calculation of W for small x. The power series in $x^{1/2}$ is most useful for small $|q|$, and the small-curvature expansion is most useful for large $|q|$.

The power series representation for W is given by (27,31)

$$W = \sum_{m=0}^{\infty} A_m (e^{j\pi/4} q x^{1/2})^m \tag{67}$$

where

$$\begin{aligned}
&A_0 = 1, A_1 = -j\pi^{1/2}, A_2 = -2\\
&A_3 = j\pi^{1/2}\left(1 + \frac{1}{4q^3}\right), A_4 = \frac{4}{3}\left(1 + \frac{1}{2q^3}\right),\\
&A_5 = -\frac{j\pi^{1/2}}{2}\left(1 + \frac{3}{4q^3}\right), A_6 = -\frac{8}{15}\left(1 + \frac{1}{q^3} + \frac{7}{32q^6}\right)\\
&A_7 = \frac{j\pi^{1/2}}{6}\left(1 + \frac{5}{4q^3} + \frac{1}{2q^6}\right), A_8 = \frac{16}{105}\left(1 + \frac{3}{2q^3} + \frac{27}{32q^6}\right)\\
&A_9 = \frac{-j\pi^{1/2}}{24}\left(1 + \frac{7}{4q^3} + \frac{5}{4q^6} + \frac{21}{64q^9}\right)
\end{aligned}$$

and

$$A_{10} = -\left(\frac{32}{945} + \frac{64}{945q^3} + \frac{11}{189q^6} + \frac{7}{270q^9}\right)$$

In the numerical results to follow, the series has been truncated at $m = 10$ because higher-order coefficients A_m are not available in the literature.

The small-curvature expansion for W is given by (31,32)

$$\begin{aligned}
W = {}& F(p) + \frac{1}{4q^3}[1 - j\sqrt{\pi p} - (1 + 2p)F(p)]\\
&+ \frac{1}{4q^6}\left[1 - j\sqrt{\pi p}(1 - p) - 2p + \frac{5p^2}{6} + \left(\frac{p^2}{2} - 1\right)F(p)\right]
\end{aligned} \tag{68}$$

where $p = jxq^2 = -jk_0d\Delta^2/2$ and the flat-earth attenuation function $F(p)$ is given by Eq. (57). When the radius a approaches ∞ (zero curvature), q approaches ∞, and W approaches F. An additional term in Eq. (68) proportional to q^{-9} has been obtained (31), but numerical results (27) indicate that it adds little improvement.

To illustrate the range of applicability of the various methods for computing W, a specific example for propagation at a frequency of 10 MHz is considered. The effective earth radius

a is taken to be 4/3 times the actual earth radius of 6368 km in order to account for normal atmospheric refraction (33). The magnitude of the normalized surface impedance $|\Delta| = 0.1$; this yields a value of 9.62 for the magnitude of q. For the phase of Δ, two values, 30° and 75°, are considered. The 30° value (phase of $q = -60°$) lies in the range encountered for a typical homogeneous earth. The 75° value (phase of $q = -15°$) lies in the highly inductive region, where a trapped surface wave is important. Numerical results for the magnitude of W as a function of distance are shown in Fig. 19, where the computations were carried out by four different methods. The oscillations in the vicinity of $d = 10$ km for the phase (Δ) = 75° curve are due to interference between the trapped surface wave and the usual ground wave.

Although the curve for phase (Δ) = 75° contains more structure than that for phase (Δ) = 30°, the range of validity of the various computational methods depends only weakly on the phase of Δ. For graphical accuracy in Fig. 19, the different methods have the following ranges of validity. The residue series calculation from Eq. (64) using 50 terms is valid for d greater than about 10 km ($x > 0.11$). This value of d or x can always be decreased by increasing the number of terms. The small-curvature formula in Eq. (68) is valid for d less than about 50 km ($x < 0.57$). The power series in Eq. (67) is valid for d less than about 1 km ($x < 0.011$). The flat-earth approximation in Eq. (57), which is the first term in Eq. (68), is valid for d less than about 15 km ($x < 0.17$). The characteristic of the flat-earth approximation for large d is an algebraic decay (d^{-2}) as opposed to the correct exponential decay of the first term of the residue series. The small-curvature formula is far superior to the power series in this example because of the large value of $|q| = 9.62$.

Further calculations (27,34) reveal the following general criteria for the method of calculation. The residue series is most useful for $x > 0.2$ regardless of the magnitude of q. For $|x| < 0.2$, the power series is better for $|q| < 1$, and the small-curvature formula is better for $|q| > 1$. The phase of q does not have to be considered in deciding which method of calculation to use for W

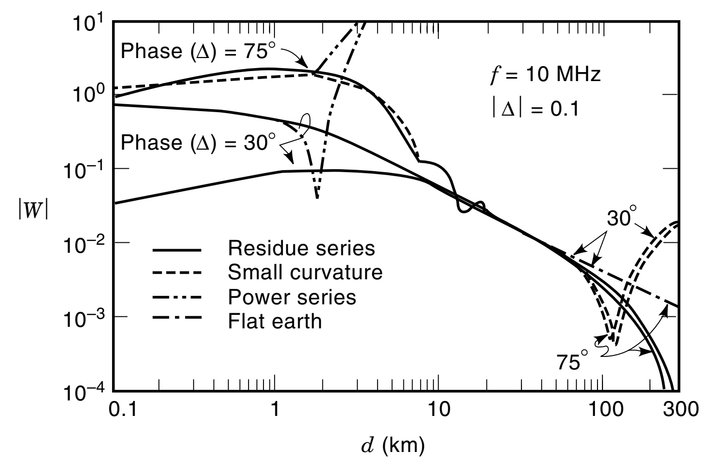

Figure 19. Magnitude of the spherical earth attenuation function as computed by various methods. (Results are shown outside their regions of validity for comparison purposes.) From Ref. 27.

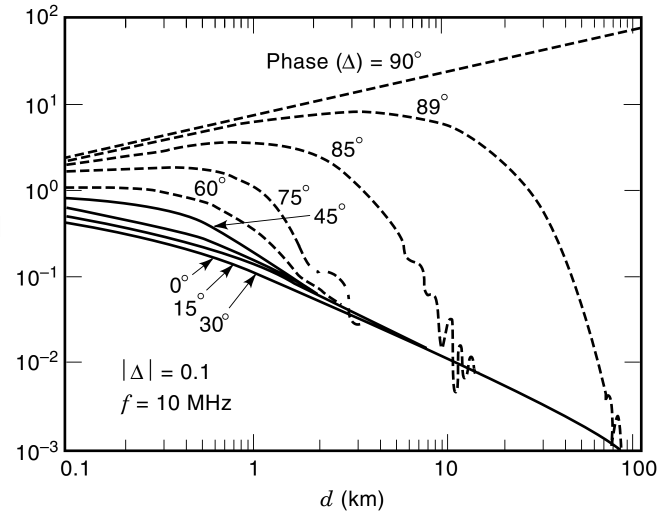

Figure 20. Magnitude of the spherical earth attenuation function for different values of the phase of the surface impedance. From Ref. 27.

The magnitude of W as a function of d is shown in Fig. 20 for a larger value of $|\Delta| = 0.2$ and for numerous values of phase (Δ). The results for $0° \leq$ phase (Δ) $\leq 45°$ show the expected smooth decay of the ground wave, but the trapped surface wave has a dominant effect for phase (Δ) > 45°. The root t_0 for the trapped surface wave, also called the Elliott mode (35), has the following asymptotic expansion (27) for large $|q|$:

$$t_0 \sim q^2 + \frac{1}{2q} + \frac{1}{8q^4} + \frac{5}{32q^7} + \frac{11}{32q^{10}} + \frac{539}{512q^{13}} - j2q^2 \exp\left(-\frac{4}{3}q^3 - 1 - \frac{7}{12q^3} - \frac{31}{48q^6} - \frac{397}{288q^9}\right) \tag{69}$$

Part of the reason for interest in inductive surface impedances is in modeling propagation over a layer of sea ice on the ocean (29).

The residue series in Eq. (64) can be generalized to the case of an elevated source and an elevated observer. For a source height of h_0 and an observer height of h, W takes the following form (28,29):

$$W = \sqrt{\frac{\pi x}{j}} \sum_{s=1}^{\infty} \frac{\exp(-jxt_s)}{t_s - q^2} G_s(y_0) G_s(y) \tag{70}$$

where

$$G_s(y) = \frac{w(t_s - y)}{w(t_s)} \tag{71}$$

$y_0 = k_0 h_0 (2/k_0 a)^{1/3}$, and $y = k_0 h (2/k_0 a)^{1/3}$. Since G_s depends on t_s, it is a function of s. G_s as given by Eq. (71) can be expanded in a power series in y (28,29):

$$G_s(y) = 1 - qy + \frac{t_s}{2}y^2 - \frac{1 + t_s q}{6}y^3 + \cdots \tag{72}$$

For low heights and small values of s, G_s can be approximated by the first two terms in Eq. (72):

$$G_s \approx 1 - qy = 1 + jk_0\,\Delta h \tag{73}$$

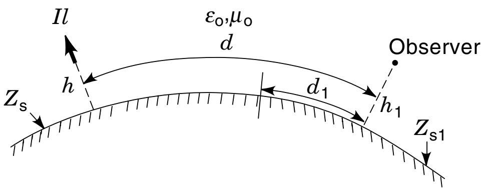

Figure 21. Propagation along a spherical earth with a change in surface impedance from Z_s to Z_{s1}.

G_s as approximated by Eq. (73) is independent of s and is equal to the height-gain function for the flat-earth model in Eq. (62).

VARIABLE TERRAIN

Although the flat-earth and spherical-earth models are useful for analyzing ground-wave propagation, many propagation paths involve variable terrain where the ground properties or surface height vary along the path. The analysis of such paths usually requires approximate or numerical methods (36–39).

Mixed Path

Mixed-path theory has been developed to analyze smooth terrain that has a change in the earth properties (conductivity and permittivity) between the source and the receiver. The mathematical theory has been developed for both a flat earth (40) and a spherical earth (41), but only the more general spherical-earth model will be considered here.

The geometry for a two-section path is shown in Fig. 21. Propagation along a three-section path (41) has also been analyzed, but will not be covered here. As in the previous section, the radial electric field E_r is normalized to the case of a flat, perfectly conducting plane:

$$E_r = \frac{-j\omega\mu_0 Il}{2\pi d} e^{-jk_0 d} W'(x, q, q_1) \tag{74}$$

where W' is the mixed-path attenuation function, $q = -j(k_0/a)^{1/3}\,\Delta$, $q_1 = -j(k_0/a)^{1/3}\,\Delta_1$, $\Delta = Z_s/\eta_0$, $\Delta_1 = Z_{s1}/\eta_0$, and a is the earth radius. Consider first the case, where the source and observer are located at the surface ($h = h_1 = 0$). In this case, the following form of W' is most useful (42,43):

$$W'(x, q, q_1) = W(x, q) + \sqrt{\frac{x}{j\pi}}(q_1 - q) \int_0^{x_1} \frac{W(x-\hat{x}, q)W(\hat{x}, q_1)}{\sqrt{\hat{x}(\hat{x}-x)}} d\hat{x}, \; d_1 > 0 \tag{75}$$

where

$$W(x, q) = \sqrt{\frac{\pi x}{j}} \sum_{s=1}^{\infty} \frac{\exp(-jxt_s)}{t_s - q^2} \tag{76}$$

$x = (k_0 a/2)^{1/3}(d/a)$, and $x_1 = (k_0 a/2)^{1/3}(d_1/a)$. The spherical-earth attenuation function in Eq. (76) is the same as that for the uniform path in Eq. (64), but the arguments are shown explicitly for use in Eq. (75). The square-root singularity in Eq. (75) is integrable, and its numerical evaluation (42) presents no difficulty. A useful alternative to Eq. (75) can be obtained by reciprocity (41):

$$W'(x, q, q_1) = W(x, q_1) + \sqrt{\frac{x}{j\pi}}(q - q_1) \int_0^{x-x_1} \frac{W(x-\hat{x}, q_1)W(\hat{x}, q)}{\sqrt{\hat{x}(\hat{x}-x)}} d\hat{x} \tag{77}$$

Equations (75) and (77) have been used to calculate W' for a variety of paths and parameters (42). Results for $|W'|$ are shown in Fig. 22 for propagation along a land-to-sea path for various lengths of the land section. The frequency is 10 MHz, the land constants are $\epsilon/\epsilon_0 = 15$ and $\sigma = 0.01$ S/m, and the sea constants are $\epsilon_1/\epsilon_0 = 80$ and $\sigma_1 = 4$ S/m. The increase in field strength that occurs in crossing the land-sea boundary has been called the recovery effect, and it has been observed experimentally by Millington (43). A similar drop in phase has been calculated (42) and observed experimentally by Pressey et al. (44). In Fig. 23, the length of the land section is fixed at 5 km, and the frequency is varied from 1 to 30 MHz. The recovery effect is most prominent at 30 MHz because the attenuation over land is so rapid at that frequency.

When either height, h or h_1, is nonzero, Eqs. (75) and (77) are still valid, but W needs to be modified by the appropriate height-gain function:

$$W(x, q) = \sqrt{\frac{\pi x}{j}} \sum_{s=1}^{\infty} \frac{\exp(-jxt_s)}{t_s - q^2} \frac{w_1(t_s - y)}{w_1(t_s)}, \quad \text{where } y = (2/k_0 a)^{1/3} k_0 h \tag{78}$$

and

$$W(x, q_1) = \sqrt{\frac{\pi x}{j}} \sum_{s=1}^{\infty} \frac{\exp(-jxt_s)}{t_s - q_1^2} \frac{w_1(t_s - y)}{w_1(t_s)}, \quad \text{where } y_1 = (2/k_0 a)^{1/3} k_0 h_1 \tag{79}$$

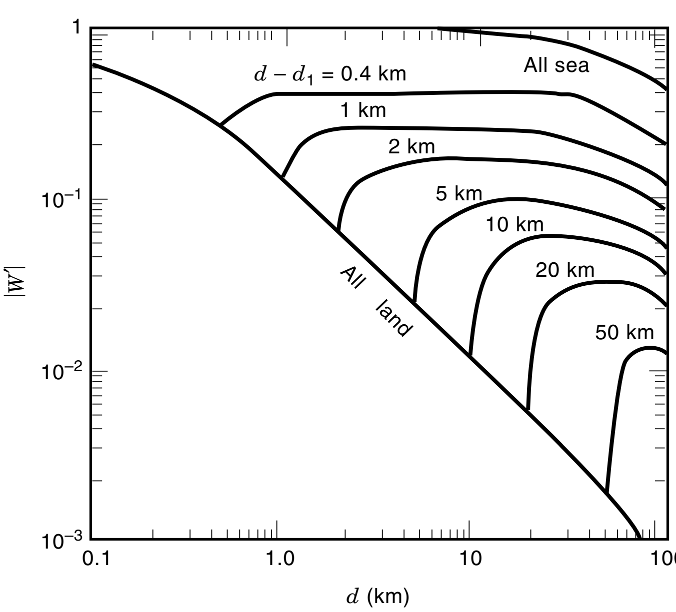

Figure 22. Magnitude of the attenuation function for a land-to-sea path for various lengths of the land section. Parameters: $f = 10$ MHz, $h = h_1 = 0$, $\epsilon/\epsilon_0 = 15$, $\sigma = 10^{-2}$ S/m, $\epsilon_1/\epsilon_0 = 80$, and $\sigma_1 = 4$ S/m. From Ref. 42.

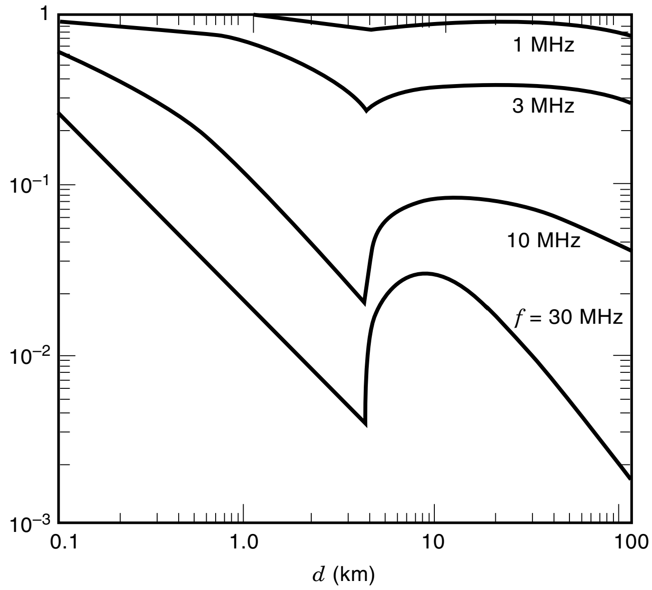

Figure 23. Magnitude of the attenuation function for a land-to-sea path for various frequencies. Parameters: $d - d_1 = 5$ km, $h = h_1 = 0$, $\epsilon/\epsilon_0 = 15$, $\sigma = 10^{-2}$ S/m, $\epsilon_1/\epsilon_0 = 80$, and $\sigma_1 = 4$ S/m. From Ref. 42.

It is possible to cast the integral forms of Eqs. (75) and (77) into a modal sum of the following form (42):

$$W'(x,q,q_1) = \sqrt{\frac{\pi x}{j}}(q_1 - q)\sum_{s=1}^{\infty}\sum_{t=1}^{\infty} \frac{\exp[-j(x-x_1)t_s - jx_1 t_r^{(1)}]}{(t_r^{(1)} - t_s)(t_s - q^2)(t_r^{(1)} - q_1^2)} \frac{w_1(t_s - y)}{w_1(t_s)} \frac{w_1(t_r^{(1)} - y_b)}{w_1(t_r^{(1)})} \quad (80)$$

where the roots $t_r^{(1)}$ satisfy the mode equation that is similar to Eq. (65):

$$w_1'(t_r^{(1)}) - q_1 w_1(t_r^{(1)}) = 0 \quad (81)$$

The double summation in Eq. (80) converges slowly when either x_1 or $x - x_1$ is small, but the roots t_s and $t_r^{(1)}$ can be computed rapidly (27).

Results for $|W'|$ are shown in Fig. 24 for propagation along a land-to-sea path for various observer heights. The length of the land section is 10 km. As many as 600 roots, t_s and $t_r^{(1)}$, were used in computing the results (42) in Fig. 24. A good confirmation of the validity of the numerical results in Fig. 24 as computed by Eq. (80) is that the curve for $h_1 = 0$ agrees with the corresponding curve in Fig. 22 as computed by Eq. (75). As the observer height h_1 is increased, the recovery effect decreases in magnitude and begins at a range beyond the land-sea boundary.

Irregular Terrain

For many propagation paths, the ground parameters and terrain height vary as a function of position along the path. Analytical methods are not general enough to handle such variations, but the integral equation approach (45,46) has been found useful for ground-wave propagation over irregular, inhomogeneous terrain. Ott's program WAGNER has been thoroughly tested and used on a wide variety of paths (47), and

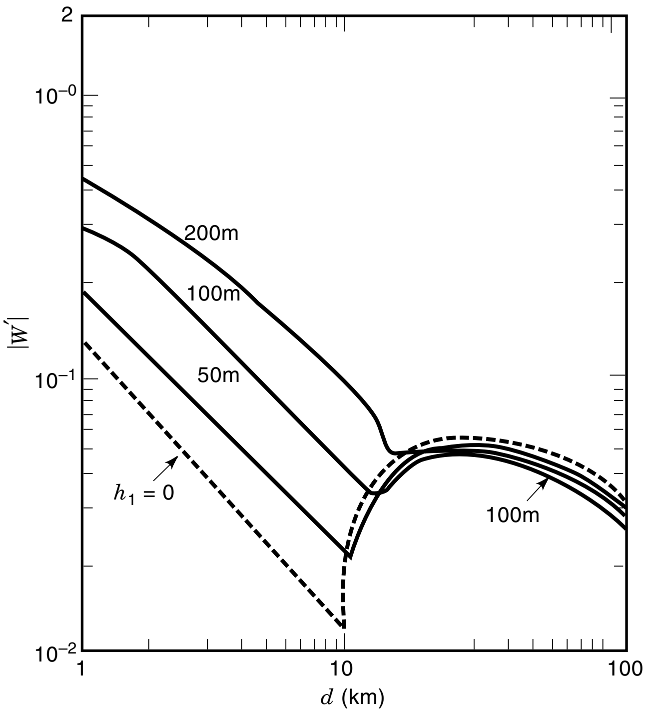

Figure 24. Magnitude of the attenuation function for a land-to-sea path for various observer heights. Parameters: $f = 10$ MHz, $d - d_1 = 10$ km, $h = 0$, $\epsilon/\epsilon_0 = 15$, $\sigma = 10^{-2}$ S/m, $\epsilon_1/\epsilon_0 = 80$, and $\sigma_1 = 4$ S/m. From Ref. 42.

Hill has generalized it to allow for an anisotropic layer over a homogeneous earth (48). The anisotropic layer is intended to model a forest layer, snow cover, or a layered earth.

The general terrain model is shown in Fig. 25. The terrain height y, the slab thickness D, and the slab and ground constitutive parameters are functions of the horizontal distance ξ from the vertical electric dipole source. The terrain is represented by a normalized surface impedance Δ (referred to the top of the slab), which is a function of the slab and ground parameters and is thus a function of ξ. The problem is first solved by considering the case where the source and observer are located at the surface ($h_a = h_r = 0$). The vertical electric

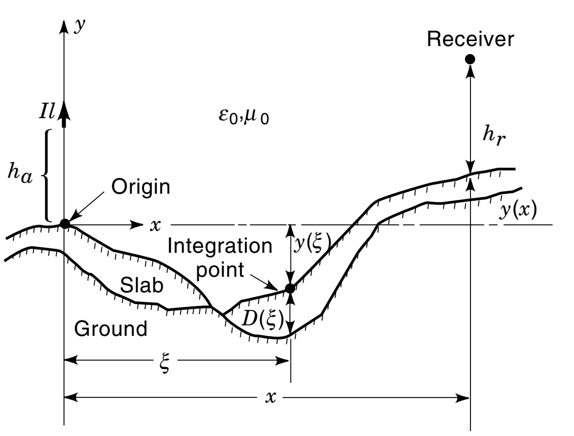

Figure 25. Geometry for the integral equation solution of propagation over irregular, inhomogeneous terrain. The slab and ground parameters can vary as a function of x, but are constant in y.

field E_y is normalized to the field of a vertical electric dipole on a conducting plane:

$$E_y = \frac{-j\omega\mu_0 Il}{2\pi x} e^{-jk_0 x} f(x) \tag{82}$$

where $f(x)$ is the attenuation to be determined from the integral equation. The integral equation is (47,48)

$$f(x) = F(x,0) - \sqrt{\frac{jk_0}{2\pi}} \int_0^x f(\xi) e^{-jk_0\phi(x,\xi)} \left(y'(\xi)F(x,\xi) - \frac{y(x)-y(\xi)}{x-\xi} + [\Delta(\xi) - \Delta_a]F(x,\xi)\right) \frac{\sqrt{x}}{\sqrt{\xi(x-\xi)}} d\xi \tag{83}$$

where

$$\phi(x,\xi) = \frac{[y(x)-y(\xi)]^2}{2x(x-\xi)} + \frac{y^2(\xi)}{2\xi} - \frac{y^2(x)}{2x}$$
$$F(x,\xi) = 1 - j\sqrt{\pi p} e^{-u} \text{ erfc } (j\sqrt{u})$$
$$p = -jk_0\Delta^2(\xi)(x-\xi)/2, u = p\left(1 - \frac{y(x)-y(\xi)}{\Delta(\xi)(x-\xi)}\right)^2$$

and $y'(\xi)$ is the slope $dy/d\xi$. The normalized surface impedance $\Delta(\xi)$ is a function of the slab and ground parameters (48):

$$\Delta(\xi) = \Delta_1 \frac{\Delta_2 + \Delta_1 \tanh(v_0 D)}{\Delta_1 + \Delta_2 \tanh(v_0 D)} \tag{84}$$

where

$$\Delta_1 = \frac{\sqrt{\epsilon_{hc} - \kappa}}{\epsilon_{hc}}, \Delta_2 = \frac{\sqrt{\epsilon_{gc} - 1}}{\epsilon_{gc}}, v_0 = jk_0\sqrt{\epsilon_{hc} - \kappa}$$
$$\epsilon_{hc} = \epsilon_h + \sigma_h/(j\omega\epsilon_0), \epsilon_{gc} = \epsilon_g + \sigma_g/(j\omega\epsilon_0),$$
$$\epsilon_{vc} = \epsilon_v + \sigma_v/(j\omega\epsilon_0), \kappa = \epsilon_{hc}/\epsilon_{vc}$$

σ_v and ϵ_v are the vertical conductivity and relative permittivity of the slab, σ_h and ϵ_h are the horizontal conductivity and relative permittivity of the slab, and σ_g and ϵ_g are the conductivity and permittivity of the ground. The ground and the slab have free-space permeability μ_0. The normalized surface impedance Δ_a is evaluated at the source.

Before discussing the numerical solution of Eq. (83), it is useful to examine the special case of a uniform path: $y(\xi) = y(x) = y'(\xi) = 0$ and $\Delta(\xi) = \Delta_a$. Thus the integrand is 0, and $f(x)$ is

$$f(x) = F(x,0) = 1 - j\sqrt{\pi p_a} e^{-p_a} \text{erfc}(j\sqrt{p_a}) \tag{85}$$

where $p_a = -jk_0\Delta_a^2 x/2$. Equation (85) agrees with the flat-earth result in Eq. (56). When either y or Δ varies along the path, the integral equation must be solved numerically. A forward-stepping solution (49) in x is used to obtain values of f at discrete values of x along the path. Since Eq. (83) is a Volterra integral equation of the second kind, the value of $f(x)$ depends only on the previously computed values of $f(\xi)$ for $\xi < x$. Physically this means that backscatter is neglected.

To account for nonzero source and receiver heights, h_a and h_r, an attenuation function f_h is determined by use of height-gain functions G_s for a slab medium (48):

$$f_h(x) = f(x)G_s(h_a)G_s(h_r) \tag{86}$$

The source and receiver can be located either in air (positive height) or in the slab (negative height). For the source or receiver in air, the height-gain function is

$$G_s(h) = 1 + jk_0\Delta h, h \geq 0 \tag{87}$$

where Δ is evaluated at the appropriate source or receiver location. For the source or receiver in the slab, the height-gain function is

$$G_s(h) = \frac{1}{\epsilon_{vc}} \frac{e^{v_0 z} + Re^{-v_0(2D+h)}}{1 + Re^{-2v_0 D}}, -D < h < 0 \tag{88}$$

where $R = (\Delta_1 - \Delta_2)/(\Delta_1 + \Delta_2)$. The limit of G_s as h approaches 0 from above is 1:

$$G_s(0^+) = 1 \tag{89}$$

The limit of G_s as h approaches 0 from below is

$$G_s(0^-) = 1/\epsilon_{vc} \tag{90}$$

This is a consequence of the continuity of normal current flow.

The numerical solution of Eq. (83) has been thoroughly studied, and comparisons with experimental results have been shown (47,48). Also, a comparison with an approximate analysis for propagation from a forest to a clearing has been made. This comparison provides an independent check because the approximate solution uses a Kirchoff integration over the vertical aperture above the forest-clearing boundary (48) in contrast to the integral equation solution, which integrates over the terrain surface. The numerical comparison for $|f_h|$ is shown in Fig. 26. The frequency is 10 MHz, the ground parameters are $\sigma_g = 10^{-2}$ S/m and $\epsilon_g = 10$, and the slab parameters are $D = 10$ m, $\sigma_h = 10^{-4}$ S/m, $\epsilon_h = 1.1$, $\sigma_v = 2.5 \times 10^{-4}$, and $\epsilon_v = 1.25$. Both the source and receiver are located at a height of 10^+ m. The approximate aperture theory shows a nonphysical jump for the receiver at the forest boundary, but the more accurate integral equation solution smooths out the jump. Away from the boundary the two solutions agree well.

For typical terrain profiles and moderate path lengths (less than 100 km), the numerical solution of Eq. (83) is reasonably accurate and efficient for frequencies up to about 10 MHz. At higher frequencies the numerical solution can become unstable and predict a nonphysical oscillatory field strength as a function of distance. Also, the computer run time, which is roughly proportional to frequency squared, can become large. To improve the stability at higher frequencies, Ott (50) has modified the integral equation and computer code and has obtained stable numerical results for frequencies up to about 100 MHz.

Knife-Edge Diffraction

At high frequencies where the wavelength is small compared to terrain features and other obstacles such as buildings, knife-edge diffraction models (51) can provide useful field predictions. The simplest model is based on a single knife edge,

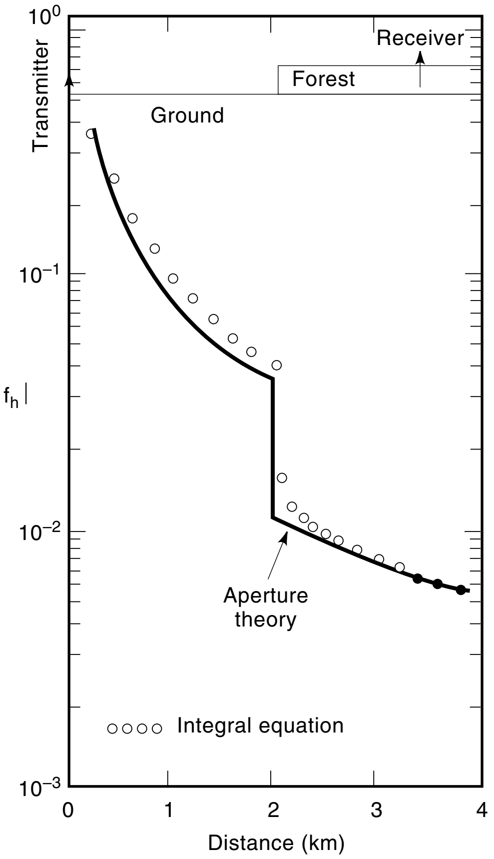

Figure 26. Propagation from a clearing to a forest at a frequency of 10 MHz. From Ref. 48.

as shown in Fig. 27. If the Kirchhoff approximation that the field in the semi-infinite aperture above the knife edge is equal to the incident field is made, then the aperture integration can be approximated with the following result for the diffracted field E_d at the receiver location R (14):

$$E_d = E_0 F(v) = E_0 \frac{1+j}{2} \int_v^\infty \exp(-j\pi t^2/2)\, dt, \quad \text{where } v = h\sqrt{\frac{2(d_1+d_2)}{\lambda_0 d_1 d_2}} \qquad (91)$$

E_0 is the free-space field in the absence of the knife edge and $F(v)$ is the complex Frensel integral. When the knife edge extends above the line connecting S and R (as in Fig. 27), h and v are positive. In this case, $|F| < 1/2$. When the top of the knife edge is below the line connecting S and R, h and v are negative. In this case, $|F| > 1/2$. As v approaches $-\infty$, $|F|$ approaches 1 in an oscillatory manner. The diffraction gain (in decibels) due to the presence of the knife edge is

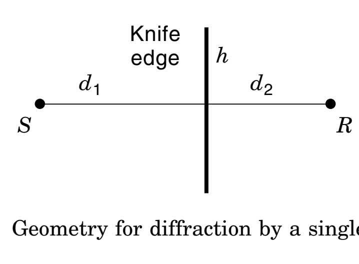

Figure 27. Geometry for diffraction by a single knife edge.

$$G_d = 20 \log_{10} |F(v)| \qquad (92)$$

To avoid computation of the Fresnel integral in Eq. (92), Lee (51) has provided simple approximations for F. The geometrical theory of diffraction (52) provides a more rigorous high-frequency method for analyzing diffraction from knife-edges and wedges, and it predicts results that depend on the polarization of the incident field.

A number of extensions to the single knife-edge model in Fig. 27 have been studied. The knife edge can be replaced by a rounded diffracting obstacle (53,54), which is a better model for broad-terrain features in some cases. Multiple knife edges (55–57) can be used to model paths with multiple diffracting obstacles. Vogler's analysis (58) is valid for an arbitrary number of knife edges, and his computer code will handle up to 10 knife edges.

BIBLIOGRAPHY

1. J. A. Stratton, *Electromagnetic Theory,* New York: McGraw-Hill, 1941.
2. R. S. Elliot, *Electromagnetics: History, Theory, and Applications,* New York: IEEE Press, 1993.
3. J. H. Bryant, *Heinrich Hertz: The Beginning of Microwaves,* New York: IEEE Press, 1988.
4. M. L. Burrows, *ELF Communications Antennas,* Stevanage, UK: IEE/Peter Peregrinus Ltd., 1978.
5. K. Davies, *Ionospheric Radio,* London, UK: IEE/Peter Peregrinus Ltd., 1989.
6. P. V. Bliokh, A. P. Nicholaenko, and Y. F. Fillippov (translated by S. Chomet), *Schumann Resonances in the Earth-Ionosphere Cavity,* Stevenage, UK: IEE/Peter Peregrinus Ltd., 1980.
7. J. N. Murphy and H. E. Parkinson, Underground mine communications, *Proc. IEEE,* **66**: 26–50, 1978.
8. J. R. Wait, Electromagnetic induction technique for locating a buried source, *IEEE Trans. Geoscience Electronics,* **9**: 95–98, 1971.
9. A. D. Watt, *VLF Radio Engineering,* Oxford, UK: Pergamon Press, 1967.
10. D. L. Schilling (ed.), *Meteor Burst Communications, Theory and Practice,* New York: Wiley, 1993.
11. K. Siwiak, *Radiowave Propagation and Antennas for Personal Communications,* Norwood, MA: Artech House, 1995.
12. R. F. Harrington, *Time-Harmonic Electromagnetic Fields,* New York: McGraw-Hill, 1961.
13. C. H. Liu and D. J. Fang, Chap. 29, Propagation, in Y. T. Lo and S. W. Lee (eds.), *Antenna Handbook: Theory, Applications, and Design,* New York: Van Nostrand Reinhold, 1988.
14. E. C. Jordan and K. G. Balmain, *Electromagnetic Waves and Radiating Systems,* Englewood Cliffs, NJ: Prentice Hall, 1968.
15. G. V. Keller and F. C. Frischnecht, *Electrical Methods in Geophysical Prospecting,* Oxford, UK: Pergamon Press, 1966.
16. D. A. Hill, Chap. 23, Antennas for geophysical applications, in Y. T. Lo and S. W. Lee (eds.), *Antenna Handbook: Theory, Applications, and Design,* New York: Van Nostrand Reinhold, 1988.
17. M. Abramowitz and I. A. Stegun, *Handbook of Mathematical Functions,* Washington, DC: National Bureau of Standards, AMS 55, 1968.
18. A. A. Kaufman and G. V. Keller, *Frequency and Transient Sounding,* Amsterdam: Elsevier, 1983.

19. J. R. Wait and D. A. Hill, Fields of a horizontal loop of arbitrary shape buried in a two-layer loop, *Rad. Sci.,* **15**: 903–912, 1980.
20. E. D. Sunde, *Earth Conduction Effects in Transmission Systems,* New York: D. Van Nostrand, 1949.
21. D. A. Hill and J. R. Wait, Subsurface electromagnetic fields of a grounded cable of finite length, *Can. J. Phys.,* **51**: 1534–1540, 1973.
22. J. R. Wait and K. P. Spies, Subsurface electromagnetic field of a line source on a conducting half-space, *Rad. Sci.,* **6**: 781–786, 1971.
23. D. A. Hill and J. R. Wait, Subsurface electric fields of a grounded cable of finite length for both frequency and time domain, *Pure Appl. Geophys.,* **111**: 2324–2332, 1973.
24. D. A. Hill, Electromagnetic surface fields of an inclined buried cable of finite length, *J. Appl. Phys.,* **44**: 5275–5279, 1973.
25. A. Banos, *Dipole Radiation in the Presence of a Conducting Half-Space,* New York: Pergamon, 1966.
26. J. R. Wait, Electromagnetic surface waves, in J. A. Saxton (ed.), *Advances in Radio Research,* London: Academic Press, pp. 157–217, 1964.
27. D. A. Hill and J. R. Wait, Ground wave attenuation function for a spherical earth with arbitrary surface impedance, *Rad. Sci.,* **15**: 637–643, 1980.
28. D. A. Hill and J. R. Wait, Excitation of the HF surface wave by vertical and horizontal antennas, *Rad. Sci.,* **14**: 767–780, 1979.
29. D. A. Hill and J. R. Wait, HF radio wave transmission over sea ice and remote sensing possibilities, *IEEE Trans. Geosci. Rem. Sens.,* **19**: 204–209, 1981.
30. J. C. P. Miller, *The Airy Integral,* Cambridge, UK: Cambridge University Press, 1946.
31. H. Bremmer, Applications of operational calculus to ground-wave propagation, particularly for long waves, *IRE Trans. Antennas Propagat.,* **6**: 267–272, 1958.
32. J. R. Wait, Radiation from a vertical antenna over a curved stratified ground, *Nat. Bur. Stand. J. Res.,* **56**: 237–244, 1956.
33. H. Bremmer, *Terrestrial Radio Waves,* New York: Elsevier, 1949.
34. K. P. Spies and J. R. Wait, On the calculation of antenna patterns for an inhomogeneous spherical earth, *Rad. Sci.,* **11**: 1361–1378, 1967.
35. R. S. Elliott, Spherical surface wave antennas, *IRE Trans. Antennas Propagat.,* **4**: 422–428, 1956.
36. G. A. Hufford, A. G. Longley, and W. A. Kissick, *A Guide to the Use of the ITS Irregular Terrain Model in the Area Prediction Mode,* National Telecommunications and Information Administration Report 82-100, April 1982.
37. N. DeMinco, *Ground-wave Analysis Model for MF Broadcast Systems,* National Telecommunications and Information Administration Report 86-203, September 1986.
38. N. DeMinco, *Automated Performance Analysis Model for Ground-wave Communication Systems,* National Telecommunications and Information Administration Report 86-209, 1986.
39. T. S. M. Maclean and Z. Wu, *Radiowave Propagation over Ground,* London: Chapman & Hall, 1993.
40. J. R. Wait, Mixed path ground wave propagation: 1. short distances, *J. Res. Nat. Bur. Stand.,* **57**: 1–15, 1956.
41. J. R. Wait, On the theory of mixed-path ground-wave propagation on a spherical earth, *J. Res. Nat. Bur. Stand.,* **65D**: 401–410, 1961.
42. D. A. Hill and J. R. Wait, HF ground wave propagation over mixed land, sea, and sea-ice paths, *IEEE Trans. Geosci. Rem. Sens.,* **19**: 210–216, 1981.
43. G. Millington, Ground wave propagation over an inhomogeneous smooth earth, Part 1, *Proc. Inst. Elec. Engr.,* **96**: 53–64, 1949.
44. B. G. Pressey, G. E. Ashwell, and C. S. Fowler, Change of phase of a low-frequency wave propagated across a coast line, *Proc. Inst. Elec. Engr.,* **103B**: 527–541, 1956.
45. G. A. Hufford, An integral equation approach to the problem of wave propagation over an irregular terrain, *Quart. J. Appl. Math.,* **9**: 391–404, 1952.
46. R. H. Ott and L. A. Berry, An alternative integral equation for propagation over irregular terrain, *Rad. Sci.,* **5**: 767–771, 1970.
47. R. H. Ott, L. E. Vogler, and G. A. Hufford, *Ground Wave Propagation over Irregular, Inhomogeneous Terrain,* National Telecommunications and Information Administration Report 79-20, 1979.
48. D. A. Hill, *HF Ground Wave Propagation over Forested and Built-up Terrain,* National Telecommunications Administration Report 82-114, December 1982.
49. C. Wagner, On the numerical solution of Volterra integral equations, *J. Math. Phys.,* **32**: 289–401, 1953.
50. R. H. Ott, RING: an integral equation for HF-VHF radio wave propagation over irregular, inhomogeneous terrain, *Rad. Sci.,* **27**: 867–882, 1992.
51. W. C. Y. Lee, *Mobile Cellular Telecommunications,* New York: McGraw-Hill, 1995.
52. G. L. James, *Geometrical Theory of Diffraction for Electromagnetic Waves,* Stevenage, UK: Peter Peregrinus, 1976.
53. J. R. Wait and A. M. Conda, Diffraction of electromagnetic waves by smooth obstacles for grazing angles, *J. Res. Nat. Bur. Stand.,* **63D**: 181–197, 1959.
54. L. E. Vogler, Radio wave diffraction by a rounded obstacle, *Rad. Sci.,* **20**: 582–590, 1985.
55. J. Epstein and D. W. Peterson, An experimental study of wave propagation at 850 Mc, *Proc. IRE,* **41**: 595–611, 1953.
56. G. Millington, R. Hewitt, and F. S. Immirizi, Double knife-edge diffraction in field-strength predictions, *Proc. IEE Monogr.,* **507E**: 419–429, 1962.
57. J. Deygout, Multiple knife-edge diffraction of microwaves, *IEEE Trans. Antennas Propagat.,* **14**: 480–489, 1966.
58. L. E. Vogler, An attenuation function for multiple knife-edge diffraction, *Rad. Sci.,* **17**: 1541–1546, 1982.

DAVID A. HILL
National Institute of Standards and Technology